Coherent control of a superconducting qubit using light

Hana K. Warner,[1] Jeffrey Holzgrafe,[1,2] Beatriz Yankelevich,[3] David Barton,[1] Stefano Poletto,[3] C. J. Xin,[1]

Neil Sinclair,[1,4] Di Zhu,[1] Eyob Sete,[3] Brandon Langley,[3] Emma Batson,[5] Marco Colangelo,[5] Amirhassan

Shams-Ansari,[1] Graham Joe,[1] Karl K. Berggren,[5] Liang Jiang,[6] Matthew Reagor,[3] and Marko Lončar*[1]

[1] *Harvard John A. Paulson School for Engineering and Applied Sciences, Cambridge, MA, USA*

[2] *Hyperlight Corporation, Cambridge, MA, USA*

[3] *Rigetti Computing, Berkeley, CA, USA*

[4] *Division of Physics, Mathematics, and Astronomy, California Institute of Technology, Pasadena, CA, USA*

[5] *Research Laboratory of Electronics, Massachusetts Institute of Technology, Cambridge, MA, USA*

[6] *Pritzker School of Molecular Engineering, University of Chicago, Chicago, IL, USA*

Quantum science and technology promise the realization of a powerful computational resource that relies on a network of quantum processors connected with low loss and low noise communication channels capable of distributing entangled states[1,2]. While superconducting microwave qubits (~3-8 GHz) operating in cryogenic environments have emerged as promising candidates for quantum processor nodes due to their strong Josephson nonlinearity and low loss[3], the information between spatially separated processor nodes will likely be carried at room temperature via telecommunication photons (200 THz) propagating in low loss optical fibers. Transduction of quantum information[4–10] between these disparate frequencies is therefore critical to leverage the advantages of each platform by interfacing quantum resources. Here, we demonstrate coherent optical control of a superconducting qubit. We achieve this by developing a microwave-optical quantum transducer that operates with up to 1.18% conversion efficiency (1.16% cooperativity) and demonstrate optically-driven Rabi oscillations (2.27 MHz) in a superconducting qubit without impacting qubit coherence times (800 ns). Finally, we discuss outlooks towards using the transducer to network quantum processor nodes.

I. INTRODUCTION

Superconducting (SC) qubits and SC quantum circuits have emerged as one of the most promising quantum computing (QC) platforms, and have been used to demonstrate processing advantages over classical supercomputers, even in the presence of system noise[11,12]. However, to reach the true potential of this platform, systems containing hundreds of logical qubits (many thousands of physical qubits) are required[13]. This is challenging since SC qubits require ultra-low temperatures to operate, and this large number of qubits would result in prohibitively large dilution refrigerators with cooling power that cannot be achieved with current technology[14]. One approach to overcome this relies on a modular computing scheme[15,16] based on a network of small scale quantum processors, each in its own refrigerator, connected with low noise and low loss quantum links. Since SC qubits can be accessed using microwave photons with frequency ~3-8 GHz range, SC quantum links between di-

lution refrigerators could be used to allow for the transmission of microwave signals. However this requires cryogenically cooled (15 mK) links between each subsystem[17], which is challenging, costly, and not scalable.

An alternative approach relies on interfacing SC qubits with photons at telecommunication frequencies (~200 THz), propagating in low-loss optical fibers. Optical photons have much higher energy than microwave photons, and thus are insensitive to thermal noise even at room temperature. Furthermore, their high carrier frequency and large bandwidth allow for wavelength-division multiplexing, resulting in 100-fold increase in the number of addressable physical qubits in a single fiber. Moreover, since silica optical fibers are weak carriers of thermal energy, they could be used to replace traditional microwave coaxial cables[18] to provide a 1000x reduction in thermal load for signals routed in and out of a refrigerator. Finally, optical fiber-based quantum links between SC processors benefit from mature classical optical communication technology and could enable efficient, low-noise, and
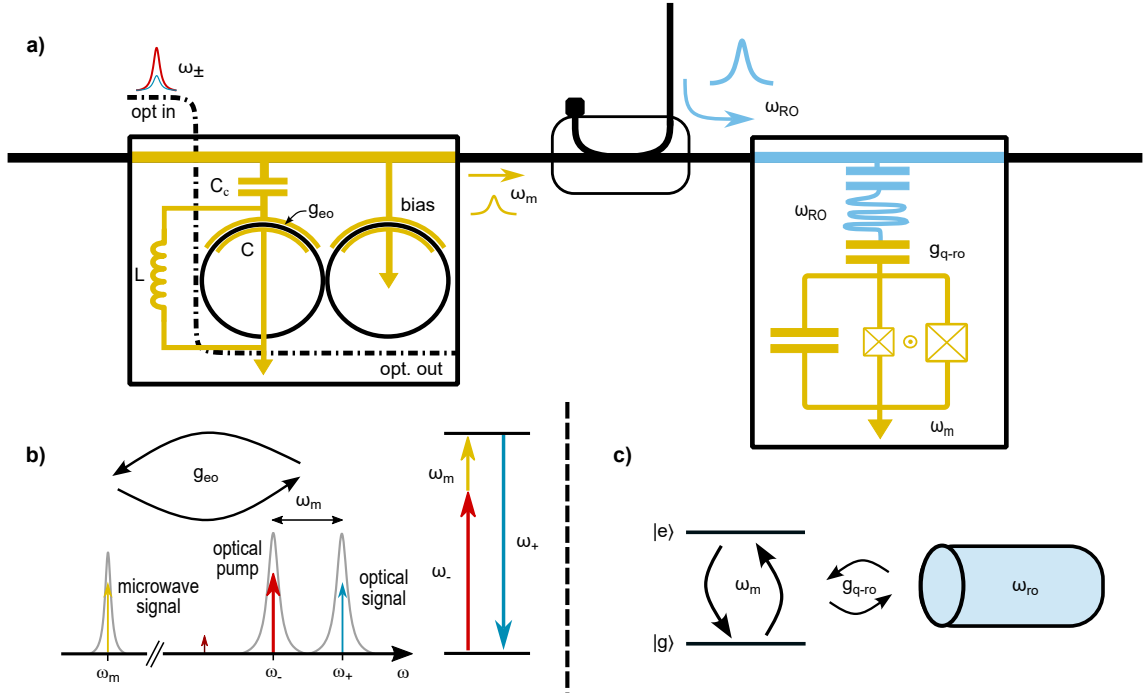
Fig. 1. Transducer-driven superconducting qubit scheme. (a) Two optical fields ($\omega_\pm$) are coupled into the transducer via a waveguide. The two modes are resonant with the transducer's hybridized optical modes which are generated by a coupled paperclip resonator capacitively coupled (C_C) to a microwave LC resonator ($\omega_m = \frac{1}{\sqrt{LC}}$). The optical modes interact in the transducer to generate a microwave tone (ω_m) via difference frequency generation using the $\chi^{(2)}$ nonlinearity in TFLN according to microwave-optical coupling rate g_{eo}. The microwave tone is then transmitted to a SC qubit chip via a coaxial cable to drive the qubit through a dispersively coupled readout resonator. We measure the qubit state by measuring the transmission of a readout pulse (ω_{ro}) generated at room temperature. (b) Schematic of cavity electro-optic transduction process. Two hybridized optical modes ($\omega_\pm$) are detuned by the microwave resonance frequency (ω_m). Energy exchange between the microwave and optical domains are mediated by the strong pump field at ω_-. (c) The qubit computational ground ($|g\rangle$) and excited ($|e\rangle$) states are separated by frequency ω_m. The qubit is dispersively coupled to a microwave readout resonator (ω_{ro}) with strength g_{q-ro}.

high rate quantum interconnects between quantum processors over kilometers[19]. This reach can be further extended by combining processors with emerging quantum-repeater based quantum networks[20].

A key component needed to interface SC qubits with light is a microwave-optical quantum transducer (MOQT), a device capable of providing a coherent, bidirectional link while preserving fragile quantum states across five orders of magnitude of energy. This is challenging due to the lack of a strong coherent nonlinearity that can bridge this vast energy gap between microwave and optical photons. Microwave-optical quantum transduction has been pursued using several approaches[2,21,22]. Piezoelectric opto-mechanical[5,23,24], membrane optomechanical[6] and cavity electro-optic[8,9,25,26] platforms have showed particular promise in recent years due to demonstrations of low noise performance[6,7,10], single photon operation[4,25,27], and bidirectional conversion[6,10,23,24,28,29]. Furthermore, recent demonstrations of optical driving[18] and readout of SC

qubits[18,30–32] demonstrate the potential to reduce passive heat load and space requirements to enable further scaling of SC processors, with high fidelity SC qubit readout in piezoelectric opto-mechanical[31] and all-optical SC qubit readout in bulk electro-optic[32] platforms illustrating the potential for near-term scaling of SC qubit systems with MOQTs.

Cavity electro-optic (CEO) MOQTs, that leverage strong Pockel's effect in materials with large χ^2 nonlinearities, are especially of interest due to the direct conversion process between the microwave and optical domains, which circumvents potential lossy, noisy, or rate-limiting intermediary modes that can limit transduction bandwidth. Among these, the thin-film lithium niobate (TFLN) photonic platform has emerged as a front runner[8,9,22] since it combines a large electro-optic (EO) coefficient ($r_{33} \approx 30$ pm/V), the ability to realize ultra-high Q optical resonators[33,34], and wafer-scale fabrication processes[35].

Despite great progress, CEO-MOQTs still require strong pump powers which can lead to increased noise and limit

the device repetition rates (in order to maintain low bath temperature)[7,25], with open questions on the influence of scattered optical light and DC flux noise on the performance of SC qubits.

Here we overcome these limitations and demonstrate a novel TFLN CEO-MOQT design and use it to demonstrate coherent optical driving of a SC qubit (Fig. 1a). The transducer is a triply-resonant system[36] that consists of an on-chip microwave LC resonator operating at frequency ω_m that is capacitively coupled via the EO effect to two coupled optical resonators that give rise to hybridized optical modes at frequencies ω_+ and $\omega_- = \omega_+ - \omega_m$[37]. This allows for a resonantly-enhanced exchange of energy between the microwave and optical modes. In our approach, an optical pump (ω_-) and idler (ω_+) interact at a CEO-MOQT to generate a microwave signal at the qubit frequency (ω_m) via a difference frequency generation process (Fig. 1b).

The microwave pulse is then transmitted via a coaxial cable to a qubit in the same refrigerator ($T_{CEO-MOQT} \approx T_{qubit} \approx 15$ mK). The qubit is dispersively coupled to a readout resonator (ω_{ro}), which allows the read-out of the qubit state via a quantum non-demolition measurement, by measuring the transmission of a readout pulse[38] (Fig. 1c). The co-operation of a thin-film CEO-MOQT and SC qubit allows us to characterize the impact of the thin-film CEO-MOQT operation on the SC qubit and validate near-term utility of TFLN electro-optic transducers for optically interfacing with SC qubits.

II. ELECTRO-OPTIC TRANSDUCER CHARACTERIZATION

Our transducer is realized using coupled optical racetrack resonators in a paperclip configuration (Fig. 2a) that supports hybridized optical modes that are delocalized between the two racetrack resonators and feature a characteristic split resonance.

The paperclip resonator allows us to maintain a low parasitic capacitance due to the small device footprint. Our optical resonators feature a 1 μm wide optical waveguide in coupling regions in order to prevent exciting higher order transverse modes. The waveguide is then adiabatically expanded to 3 μm in straight sections of the cavities to minimize optical losses caused by sidewall roughness ($\kappa_{o,i}/2\pi \approx 25$ MHz, $\kappa_o/2\pi \approx 80$ MHz). Waveguides are patterned using a neg-

ative tone e-beam resist (hydrogen silsesquioxane FOx-16) and etched using Ar+ plasma ion etching. Devices are annealed after etching in a 520°C oxygen environment to mitigate defects in as-received lithium niobate or accumulated during the etching process. They are then cladded with IC-PECVD silicon dioxide and re-annealed at 520°C in O_2 to mitigate hydrogen defects in the device oxide cladding that result in excess optical losses[34]. Next, windows in our oxide layer surrounding optical waveguides are created using a combination of Ar$^+$ and C_3F_8 reactive ion etching. Nb is then sputtered and patterned using negative tone photoresist (SPR 700-1.0) and etched using C_3F_8 reactive ion etching to create superconducting electrodes needed to realize our microwave LC resonator and transmission lines. This allows us to use a plateau-like electrode geometry (Fig. 2b), where our electrodes are in direct contact with the r_{33} axis of the $LiNbO_3$ crystal, which enhances the microwave-optical field overlap. This improves our simulated microwave-optical coupling rate by 40% when compared to a fully cladded device structure and increases the rate of coherent exchange of energy between optical and microwave signals (see Extended Data Fig. 8). Furthermore, direct contact between LN and metal is known to mitigate charge screening effects and DC bias drift[39,40], enabling a more stable operation at the triple-resonance condition.

A 191 μm mismatch in the length of the coupled racetrack resonators is introduced to create a 4 GHz (31 pm) difference in FSR which results in a Vernier effect for our optical modes (Fig. 2c) with 5 nm periodicity. This results in different coupling and frequency splitting (anti-crossing) for different modes and ensures that some of the hybridize mode pairs feature a resonance split close to the microwave resonator frequency. Then, moderate DC bias voltages ($V_{DC} < 50$) compatible with our cryogenic bias-tee at the mixing chamber plate of the refrigerator can be applied to bias the electrode to fine-tune the resonance splitting via the EO effect and achieve our triple resonance condition (Fig. 2d).

Our LC microwave resonator is designed to be a few MHz blue-detuned from the desired microwave frequency $\omega_m = \omega_+ - \omega_-$ to compensate for red-shifting and broadening it experiences under strong optical pumping due to small but finite optical absorption in our superconductor. The device reported here has a microwave frequency $\omega_m/2\pi \leq 3.71$ GHz
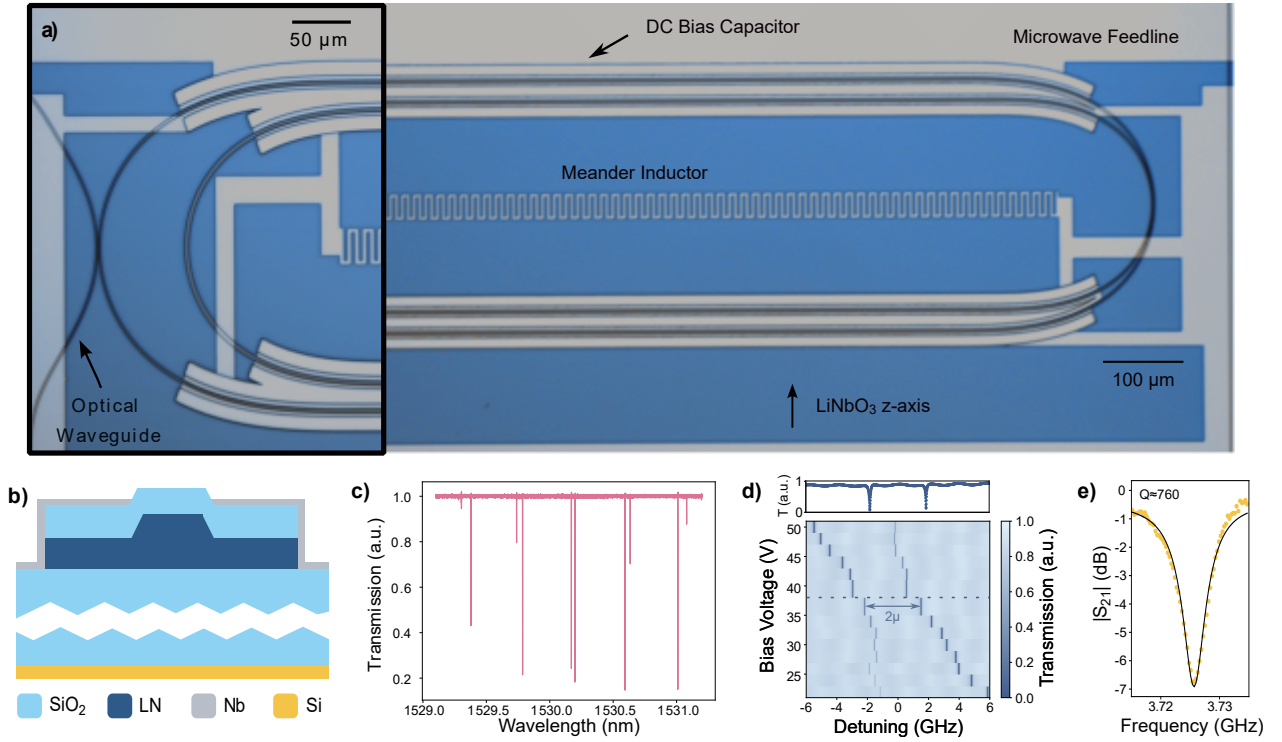
Fig. 2. CEO-MOQT. (a) Optical micrograph of transducer. A niobium (Nb) microwave LC resonator (silver) is capacitively coupled to two hybridized lithium niobate racetrack resonators in a paperclip geometry (black) to coherently exchange energy between the microwave and optical domains using the resonantly-enhanced electro-optic effect in lithium niobate. This geometry allows us to have a small device footprint to lower parasitic capacitance. The device is cladded with IC-PECVD silica to aid with thermal dissipation and mitigate optical losses due to electrical crossovers. The microwave signal is read out via a transmission line (top), and the optical signal is collected via optical grating couplers (See Extended Data Fig. 7). The optical racetrack resonators adiabatically taper from 1 μm in coupling regions to 3 μm in the straight section of the racetrack to reduce sidewall scattering losses while supporting only the fundamental transverse mode (inset). (b) Drawing of device cross-section. Our optical waveguides are gated in a plateau-like electrode geometry to directly contact our Nb electrodes with the z-axis of the LN crystal, thus benefiting from the large Pockel's coefficient ($r_{33} \approx 30$ pm/V). This improves microwave-optical field overlap, and thus the single photon coupling rate between our microwave and optical modes. (c) The nested paperclip geometry results in a Vernier effect with 5 nm periodicity and ensures the existence of a pair of hybridized optical modes with splitting similar to the microwave resonant frequency. (d) We can then ensure that we operate at the triple-resonance point by controlling the optical detuning with a voltage bias ($2\mu \approx 3.5$ GHz) in order to match (e) our microwave resonator frequency ($\omega_m \approx 3.7$ GHz).

(Fig 2e) and a minimal optical mode splitting $2\mu \approx 3.5$ GHz (Fig 2d). We operated our device with a DC voltage bias $V_{DC} \approx 36$ V.

To characterize the efficiency of the bidirectional transduction process (η), we excite the paperclip resonator with a strong optical pump resonant with our red optical mode ($\omega_- \approx 193$ THz). For optical-to-microwave conversion, we also excite the paperclip resonator with a weaker optical idler resonant with the blue optical mode (ω_+), that is derived from the pump using a single sideband modulator (SSBM). The idler power is 20 dB lower than the pump power in order to remain in the red-pumping regime. The two modes interact in the transducer to generate a microwave signal at the microwave resonator frequency via difference frequency generation ($\omega_m = \omega_+ - \omega_-$), which we measure on a network analyzer after ~ 70 dB of link gain. In the microwave-optical conversion regime, a microwave tone generated by the network

analyzer interacts with the red pump to generate a blue optical signal via sum frequency generation ($\omega_+ = \omega_- + \omega_m$). The on-chip microwave power is kept low, with uniform power $P_m \approx -80$ dBm. We measure the beatnote of the optical signal against an optical pump on a calibrated InGaAs detector in order to extract the flux of the optical signal and characterize conversion in the microwave-optical regime. The device is characterized in the continuous wave (CW) and pulsed optical regimes. The pulsed regime allows for larger peak optical powers to be applied while avoiding negative photorefractive effects or thermal bath heating. Square optical pulses are generated by modulating the state of our optical fields by an acousto-optic modulator (AOM) driven by an arbitrary-waveform generator (AWG). Pulses are then amplified by an erbium-doped fiber amplifier (EDFA) before being sent to the transducer. In the pulsed-optical regime, we choose our optical pulse width and duty cycle to maintain a low thermal

bath temperature ($T_{bath} \leq 30$ mK). See Extended Data Fig. 9 for further details on the measurement system.

In Fig. 3a, we show the on-chip conversion efficiency for different peak on-chip optical powers and duty cycles in the range 2-15%. For pulsed measurements, we maintained a pulse width of 150 ns with pulse frequency changing from 1 MHz to 200 kHz. Smaller duty cycle is beneficial for keeping average optical power in the refrigerator low, while a high repetition rate can result in faster operation of the transducer. We extract the conversion efficiency per-microwatt of pump to be ~0.05%/µW in the linear operating regime of our superconductor. In current experiments, the peak conversion efficiency measured both in the microwave → optical and optical → microwave conversion regimes is $\eta \approx 1.18\%$ for -13.8 dBm (44.2 µW) of on-chip optical power (Fig. 3a). We note that this is a 400-fold improvement over our previous result[8] and a 500x improvement in conversion per µW of pump power when compared to other integrated photonics EO transducers[7,9]. Our transducer also features a bidirectional 3dB bandwidth up to 30 MHz (Fig. 3b). This is extracted by sweeping the frequency applied to the SSBM using a network analyzer. The roll-off in converted power measured at high optical pump powers corresponds to a distortion of our microwave resonator due to finite absorption of the superconductor resulting in nonlinear behaviour, as well as drift in our triple-resonance condition during measurement.

From efficiency and linewidth measurements, we can extract the microwave-optical coupling rate (g_{eo}) and cooperativity (C) in order to understand the coherence of our system, given $C = \frac{4g_{eo}^2 n_-}{\kappa_+ \kappa_m}$. We find that the $g_{eo}/2\pi \approx 945$ Hz with cooperativity up to 1.16%.

III. TRANSDUCER-QUBIT INTERCONNECT

We use the transducer to control a SC qubit using microwave signals generated by the transducer from optical inputs. Here, we drive an aluminum split-transmon qubit through the readout resonator. We operate the transducer in a classical red pumping regime to coherently convert an optical tone (idler) into a microwave tone in an interaction mediated by a strong optical pump using the pulse sequence depicted in Figure 4a. Here, an arbitrary waveform generator
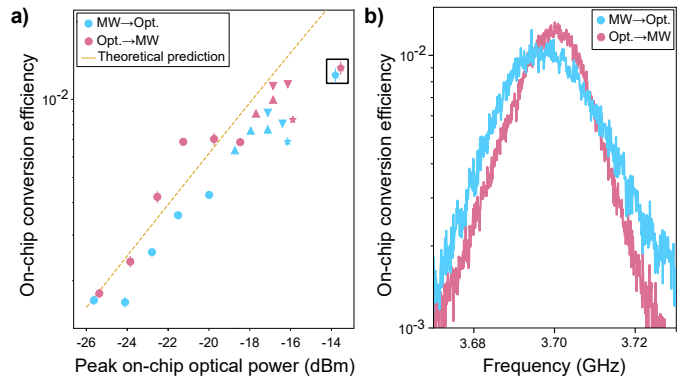

Fig. 3. (a) On-chip conversion efficiency for MW→Opt. (blue, sum frequency generation) and Opt.→MW (pink, difference frequency generation) measured for different peak on chip optical pump powers. The roll-off in conversion efficiency is attributed to optical-pump induced quasi-particle generation in our superconductor resulting in excess loss in our microwave resonator and drift away from the triply resonant condition. ∘ markers correspond to CW optical signals, whereas other shapes correspond to a 150 ns pulse with △ 1 MHz repetition rate (15% duty cycle), ▽ 500 kHz repetition rate (7.5% duty cycle), ⋆ 333 kHz repetition rate (5% duty cycle), and ⌂ 200 kHz repetition rate (2% duty cycle). The theoretical peak conversion efficiency assuming uniform optical and microwave loss rates is plotted as a dotted gold line. (b) A frequency-dependent efficiency sweep for a 150 ns pulse with 200 kHz duty cycle is highlighted in the black box in (a).

(AWG) triggered by the qubit control board (Radio Frequency System on a Chip, RFSoC) is used to gate the optical pulses used to generate the microwave drive signal. The RFSoC then sends a readout pulse to the qubit to measure the qubit state after excitation. The optical pulse length is chosen to be much longer than the microwave resonator linewidth ($\tau_{mw} \approx$ 10 ns) so the generated microwave pulse width matches the optical pulse. We use a 100 µs repetition time between events to be consistent with baseline, traditional RF qubit measurements (see Extended Data Fig. 10) while maintaining a low bath temperature (T≈14 mK).

We perform qubit spectroscopy and Rabi oscillation measurements. We first perform continuous wave (CW) qubit spectroscopy using a CW microwave tone generated by the transducer to excite the qubit population (Fig 4b) to verify excitation transfer between the transducer and qubit and determine the transducer output power needed to excite the qubit. We fit a Lorentzian to extract the qubit linewidth $\kappa_q/2\pi = 645$ kHz.

Next, we perform Rabi oscillation measurements in the power (Fig. 4c) and time (Fig. 4d-e) domains and extract parameters needed to impart a π-pulse to the qubit. For optically-driven qubit power-Rabi measurements, we keep a 100 ns optical pulse width and uniform pump power (P_{ω_-})
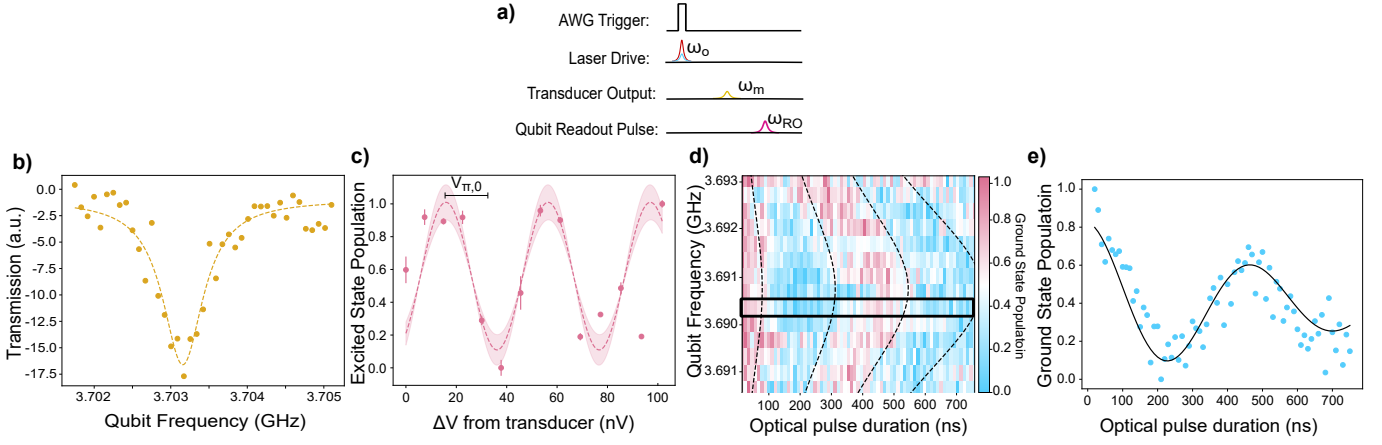
Fig. 4. Optical control of superconducting qubits. (a) Pulse sequence for pulsed transducer-driven qubit measurements. A trigger is sent from the room-temperature qubit control electronics to trigger the optical pulses. Optical pulses at the transducer generate a microwave pulse of approximately equal pulse width. The pulse is sent to the qubit, after which a readout pulse is generated at room temperature, transmitted through the qubit readout resonator, and measured in order to extract the qubit state. See Sup. VI C for full details. (b) Continuous wave qubit spectroscopy using ~328 nV microwave signal generated by the transducer. Flux biasing of the qubit is used to sweep the qubit frequency into resonance with the transducer signal. Population is read out via the resonator, where the transmission dip corresponds to a shift of the dispersively-coupled readout resonator. We measure the qubit to be at 3.703 GHz with a 645 kHz linewidth. (c) Optically driven qubit power Rabi oscillations using the pulse sequence described in (a) with 100 ns pulses. The optical on-chip pump power is kept constant at $P_{pk} = 7 \pm 0.5$ μW. The idler's optical power is swept from 400 to 500 nW, which corresponds to qubit drive voltages from 856 to 958 nV. From our measurements, we fit the Rabi oscillation and evaluate a Rabi π-pulse amplitude $V_\pi \propto 20.28 \pm 0.035$ nV satisfied for integer multiples of $V_{\pi,n}$. (d-e) Optically driven qubit time-Rabi oscillations. We fix the power in the optical pump and idler and sweep the width of the optical pulses to measure the corresponding change in qubit population. (d) We flux bias the qubit to sweep the detuning of the qubit from the optically-generated microwave tone in a characteristic chevron profile. Dotted lines are the theoretical prediction of Rabi frequency as a function of detuning following $\Omega'_R = \sqrt{\Omega_R^2 + \delta^2}$ where Ω'_R is the Rabi frequency at detuning δ given resonant Rabi frequency Ω_R. The population for different pulse widths near the optimal bias is shown in (e) where we measure a Rabi frequency of 2.27 MHz by fitting a Rabi oscillation with a time decay.

while linearly increasing the optical power in the blue sideband (P_{ω_+}) arriving at the transducer to linearly increases the microwave power arriving to the qubit (Fig. 4c). This results in a π-pulse voltage amplitude $V_\pi = nV_{\pi,0}$ where $V_{\pi,0} = 20.28$ nV and n is an integer extracted by fitting the Rabi oscillation to $P_{Rabi} = A sin(2\pi V/(2V_\pi)) + P_b$ for voltage V, background P_b, and π-pulse V_π. Some output power instability (>3 dB measured before and after some successive measurements) due to power dependent drifts in our system motivated further measurements in the time-Rabi domain in order to maintain more uniform power at our single-sideband modulator and device.

For optically-driven time-Rabi measurements (Fig. 4d,e) we maintain uniform pump and idler power and sweep the optical pulse width in order to change the width of the microwave pulse arriving to the qubits ($P_{MW} = -115.8 \pm 0.4$ dBm, $V_{MW}=362.6\pm16.5$ nV). The flux bias is swept to bias the qubit to different frequencies in order to measure the qubit excitation relative to the transducer frequency in a chevron-type measurement, where the Rabi frequency (Ω'_r) changes as a function of detuning δ by $\Omega'_R = \sqrt{\Omega_r^2 + \delta^2}$ (dotted lines

in Fig. 4d). We fit the Rabi oscillations according to $P_{Rabi} = Ae^{-t/\tau} sin(2\pi t/(2T_\pi)) + P_b$ to extract a π shift to qubit for pulse width T_π, characteristic decay τ, and offset P_b and measure $T_\pi \propto 220$ ns with $\Omega_R/2\pi = 2.27$ MHz near the transducer frequency.

The characteristic decay $\tau = 800$ ns measured for optically-driven time rabi measurements matches the coherence time measured in RF qubit measurements ($T_2^* = 800$ ns). Since $\tau \approx T_2^*$, this suggests that the transducer drive is not limiting the coherence time of the qubit. In general, optically pumping the transducer has little effect on the qubit lifetime ($T_{1,pump} \approx T_{1,RF} \approx 8$ μs), coherence time ($T_{2,pump}^* \approx 800$ ns), or readout fidelity ($F \approx 0.7$) when compared to results from RF-driven measurements (see Extended Data Figs. 10,12 for full details). This suggests that operating the transducer within the reported regimes does not degrade qubit performance. Furthermore, since we measure a reduced $\tau_{rabi,RF} \approx 200$ ns $< \tau_{rabi,optical}$ for RF-driven qubit time-Rabi measurements, this suggests that optically-driving the qubit with the transducer allows us to circumvent some decoherence sources in our room-temperature qubit control electronics.

IV. DISCUSSIONS AND OUTLOOK

We demonstrate a CEO-MOQT with high per-microwatt conversion efficiency in the linear regime of our SC resonator ($\%\eta/\mu W = 0.05$) driven with up to 44 μW for a peak efficiency $\eta = 1.18\%$, cooperativity $C = 1.16\%$, and $g_{eo}/2\pi = 945$ Hz used for coherent optical-driving of a SC qubit. Further device improvements to decrease microwave losses via a single-sided resonator design on silicon, decrease optical losses by improving optical coupling, and lower-loss SiO_2 cladding can result in orders of magnitude improvement to device performance. Furthermore, the increased optical bandwidth when compared to the microwave domain can be leveraged with a flux tunable microwave cavity[26] or fast flux biasing of the qubits[44]. Measurement improvements, such as a phase lock loop between the qubit readout electronics (or future transducers at the readout frequency) and the pump driving tone can allow for phase control of the qubits and more intricate gate operations between qubit nodes. Careful pulse shaping of our optical pump fields to control the generated microwave pulse shape or a tunable coupler on the qubit can improve signal capture between the optically-generated microwave tone and the qubits. This work, when combined with recent demonstrations of optical readout of SC qubits[31,32], provide a path towards all-optical coherent control and readout of superconducting quantum processors.

Futhermore, while the CEO-MOQT discussed in this article operates in the low cooperativity regime with modest conversion efficiency, it can already be used to network SC qubits using a heralded remote-entanglement protocols[15,41]. A proposed single-link architecture for remote entanglement between two SC qubits is shown in Fig 5a. Two transducers in two separate nodes are pumped on the blue optical mode (ω_+) in the weak-cooperativity regime in order to generate correlated microwave (ω_m) and optical (ω_-) photon pairs via spontaneous parametric down conversion (SPDC) without significant multi-photon events (Fig 5a, inset). The microwave state can be collected in a superconducting qubit network located within each node. Passing the two optical signal photons through a beamsplitter after filtering the pump pulse erases the which-path information and ensures, in the regime where $p_{multi} << 1$, the detection of a signal optical photon heralds the creation of an entangled Bell state at

the superconducting qubits, which can then be used an entanglement resource at the processor.

To date, generation of entangled microwave and optical photon pairs have been demonstrated in bulk electro-optic[25] and thin-film piezo-optomechanical[4,27] transduction platforms. We analyze the architecture proposed in Fig. 5a for current device performance and practical improvements to the device and measurement setup, examining key metrics of entanglement generation rate (R_{ent}) and link fidelity (F) due to their importance to enabling entanglement distillation between the two processor nodes. In general, entanglement distillation requires that the entanglement rate is higher than the decoherence timescale of the node's quantum processor; furthermore, increasing raw link fidelity in the system will reduce the total overhead in processor events for entanglement distillation.

The near term outlook to employing such an architecture is reported in the table in Fig. 5b assuming 40 μW pump power, 1 MHz repetition rate, and 150 ns pulse width ($P_{avg} = 7$ μW). We estimate that photon pairs can be produced at a rate of 0.68 Hz with the device discussed in this article. This rate can be further improved to $R_{ent} > 4.5$ Hz by reducing on-chip optical losses to $\kappa_o/2\pi \leq 50$ MHz using a lower-loss oxide[34] or air-cladding devices[33] and reducing on-chip microwave losses to $\kappa_m/2\pi = 10$ MHz by moving to a single-sided microwave LC resonator geometry. Reducing off-chip coupling losses to 1 dB with demonstrated low-loss, tapered fiber techniques[45] would result in significant increase in entanglement rates ($R_{ent} = 3.5$ kHz). Other system improvements, such as integrating pump filters on-chip[46], could further improve pair generation rates by eliminating high loss expected from the cascaded bulk filter cavities required to extinguish the pump photon. In the current system architecture, link fidelity is low (F=0.18) due to high (~3 dB) loss between the CEO-MOQT and SC qubits due to a frequency mismatch with bulk electronic components resulting in high reflection of our microwave signal before arriving to the qubits. Fidelity can be easily improved (F=0.83) by matching the bulk electronic and device frequencies to significantly reduce transmission losses ($P_{loss,est} = 0.3$ dB) or by co-packaging the transducer and qubits (F=0.90) with flipped-chip bonding techniques ($P_{loss,est} < 0.1$ dB)[47]. Microwave-optical quantum transducers, like the one described here, can enable the
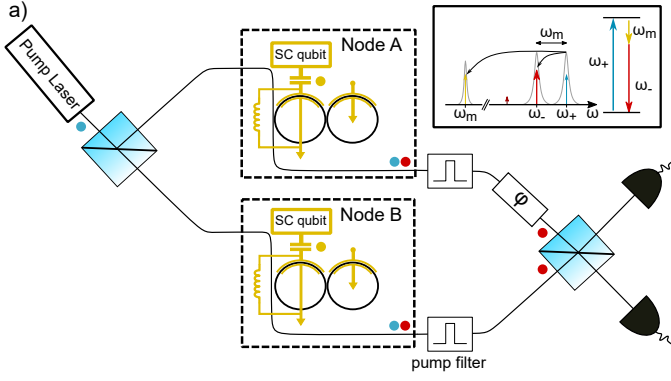
Table 1: Microwave-optical pair generation outlook

	$\kappa_{m}/2\pi$ (MHz)	$\kappa_{o}/2\pi$ (MHz)	η_{opt} (dB)	η^{t-q}_{MW} (dB)	R_{ent} (Hz)	F_{link}
This work	15	80	22	3	0.68	0.18
Reduced on-chip losses and frequency matching to bulk electronics	10	50	22	0.3	4.5	0.83
Reduced total losses	10	50	11	0.1	3.5×10^3	0.90

Fig. 5. Outlook towards remote entanglement of SC qubits using an optical channel. (a) Proposed DLCZ scheme[41] optical generation of remote entanglement between superconducting qubits. A pump laser resonant with the blue optical mode (ω_+) can induce spontaneous parametric down conversion (SPDC) to create correlated microwave and optical photon pairs in two transducers in two remote nodes. Combining the output optical channel of both nodes on a beamsplitter after pump filtering erases the which-path information so that detection of a single signal photon generates entangled microwave Bell states across the two nodes. (b) Outlook towards entanglement rates ($R_{ent} = \eta_o p_{pair} R$ for optical detection efficiency η_o, pair generation probability $p = 4\frac{g_{eo}^2}{\kappa_o^2} N_{pump}$), and entanglement attempt repitition rate R) and microwave link fidelities ($F^{t-q}_{link} = 1 - p_{multi} - 2P_m - \frac{3}{2}P_{loss} - P_{false} - P_{phase}$ for multi-photon events p_{multi}, microwave noise photons P_m, transmission losses between the transducer and qubits $P_{loss} = \eta^{t-q}_{mw}$, false detection events P_{false}, and phase errors P_{phase}) between the transducer and qubit. Here, we assume 7 μW average optical power ($P_{pk} = 40$ μW) with a 1 MHz repetition rate to keep multi-photon events low ($p_{multi} \leq 0.02$). We assume similar noise statistics for this pump power ($p_m \approx 0.02$) to other LN CEO-MOQTs reported in[7,10], use of low false detection rate ($R_{false} < 10$ Hz[42]) superconducting nano-wire single photon detectors with $P_{false} < 10^{-3}$ and minimal phase errors ($P_{phase} \approx 0.01$) using active stabilization of the interferometer path length[43] . We evaluate estimated pair generation detection rates for the work demonstrated here as how reductions to on- and off-chip microwave and optical losses can lead to significant improvements to detection rates and fidelities between the two subsystems.

networking of processors across multiple cryostats, eliminating volumetric constraints that currently exist in these systems. This can allow for low thermal-load driving and readout of superconducting devices and entanglement generation between qubit nodes via teleportation. These resources can be routed between processor nodes at kilometer length scales. Furthermore, up-conversion from the microwave-optical domain can allow SC qubits to interface with long-lifetime solid state quantum memories and repeaters to enable processing in a "quantum-cloud"[48,49], futher extending the capabilities of SC quantum processors.

[1] Kimble, H. J. The quantum internet. *Nature* **453**, 1023–1030 (2008). Number: 7198 Publisher: Nature Publishing Group.

[2] Clerk, A. A., Lehnert, K. W., Bertet, P., Petta, J. R. & Nakamura, Y. Hybrid quantum systems with circuit quantum electrodynamics. *Nature Physics* **16**, 257–267 (2020). Number: 3 Publisher: Nature Publishing Group.

[3] Kjaergaard, M. *et al.* Superconducting Qubits: Current State of Play. *Annual Review of Condensed Matter Physics* **11**, 369–395 (2020). _eprint: https://doi.org/10.1146/annurev-conmatphys-031119-050605.

[4] Jiang, W. *et al.* Optically heralded microwave photon addition (2023).

[5] Mirhosseini, M., Sipahigil, A., Kalaee, M. & Painter, O. Superconducting qubit to optical photon transduction. *Nature* **588**, 599–603 (2020).

[6] Brubaker, B. *et al.* Optomechanical Ground-State Cooling in a Continuous and Efficient Electro-Optic Transducer. *Physical Review X* **12**, 021062 (2022). Publisher: American Physical Society.

[7] Xu, Y. *et al.* Bidirectional interconversion of microwave and light with thin-film lithium niobate. *Nature Communications* **12**, 4453 (2021). Number: 1 Publisher: Nature Publishing Group.

[8] Holzgrafe, J. *et al.* Cavity electro-optics in thin-film lithium niobate for efficient microwave-to-optical transduction. *Optica* **7**, 1714–1720 (2020). Publisher: Optica Publishing Group.

[9] McKenna, T. P. *et al.* Cryogenic microwave-to-optical conversion using a triply resonant lithium-niobate-on-sapphire transducer. *Optica* **7**, 1737–1745 (2020). Publisher: Optica Publishing Group.

[10] Hease, W. *et al.* Bidirectional Electro-Optic Wavelength Conversion in the Quantum Ground State. *PRX Quantum* **1**, 020315

[11] Arute, F. *et al.* Quantum supremacy using a programmable superconducting processor. *Nature* **574**, 505–510 (2019). Number: 7779 Publisher: Nature Publishing Group.

[12] Kim, Y. *et al.* Evidence for the utility of quantum computing before fault tolerance. *Nature* **618**, 500–505 (2023). Number: 7965 Publisher: Nature Publishing Group.

[13] Gambetta, J. M., Chow, J. M. & Steffen, M. Building logical qubits in a superconducting quantum computing system. *npj Quantum Information* **3**, 1–7 (2017). Number: 1 Publisher: Nature Publishing Group.

[14] Krinner, S. *et al.* Engineering cryogenic setups for 100-qubit scale superconducting circuit systems. *EPJ Quantum Technology* **6**, 1–29 (2019). Number: 1 Publisher: SpringerOpen.

[15] Krastanov, S. *et al.* Optically Heralded Entanglement of Superconducting Systems in Quantum Networks. *Physical Review Letters* **127**, 040503 (2021). Publisher: American Physical Society.

[16] Zhong, C., Han, X. & Jiang, L. Microwave and optical entanglement for quantum transduction with electro-optomechanics. *Phys. Rev. Appl.* **18**, 054061 (2022).

[17] Storz, S. *et al.* Loophole-free Bell inequality violation with superconducting circuits. *Nature* **617**, 265–270 (2023). Number: 7960 Publisher: Nature Publishing Group.

[18] Lecocq, F. *et al.* Control and readout of a superconducting qubit using a photonic link. *Nature* **591**, 575–579 (2021). Number: 7851 Publisher: Nature Publishing Group.

[19] Bersin, E. *et al.* Development of a Boston-area 50-km fiber quantum network testbed. *arxiv.org/pdf/2307.15696* (2023).

[20] Reiserer, A., Kalb, N., Rempe, G. & Ritter, S. A quantum gate between a flying optical photon and a single trapped atom. *Nature* **508**, 237–240 (2014). Number: 7495 Publisher: Nature Publishing Group.

[21] Lauk, N. *et al.* Perspectives on quantum transduction. *Quantum Science and Technology* **5**, 020501 (2020).

[22] Han, X., Fu, W., Zou, C.-L., Jiang, L. & Tang, H. X. Microwave-optical quantum frequency conversion. *Optica* **8**, 1050 (2021).

[23] Jiang, W. *et al.* Efficient bidirectional piezo-optomechanical transduction between microwave and optical frequency. *Nature Communications* **11**, 1166 (2020). Number: 1 Publisher: Nature Publishing Group.

[24] Weaver, M. J. *et al.* An integrated microwave-to-optics interface for scalable quantum computing (2022). ArXiv:2210.15702 [physics, physics:quant-ph].

[25] Sahu, R. *et al.* Entangling microwaves with light. *Science* **380**, 718–721 (2023). Publisher: American Association for the Advancement of Science.

[26] Xu, M., Han, X., Fu, W., Zou, C.-L. & Tang, H. X. Frequency-tunable high-Q superconducting resonators via wireless control of nonlinear kinetic inductance. *Applied Physics Letters* **114**, 192601 (2019).

[27] Meesala, S. *et al.* Non-classical microwave-optical photon pair generation with a chip-scale transducer (2023). ArXiv:2303.17684 [quant-ph].

[28] Fan, L. *et al.* Superconducting cavity electro-optics: A platform for coherent photon conversion between superconducting and photonic circuits. *Science Advances* **4**, eaar4994 (2018). Publisher: American Association for the Advancement of Science.

[29] Andrews, R. W. *et al.* Bidirectional and efficient conversion between microwave and optical light. *Nature Physics* **10**, 321–326 (2014). Number: 4 Publisher: Nature Publishing Group.

[30] Delaney, R. D. *et al.* Superconducting-qubit readout via low-backaction electro-optic transduction. *Nature* **606**, 489–493 (2022). Number: 7914 Publisher: Nature Publishing Group.

[31] van Thiel, T. C. *et al.* High-fidelity optical readout of a superconducting qubit using a scalable piezo-optomechanical transducer (2023). ArXiv:2310.06026 [quant-ph].

[32] Arnold, G. *et al.* All-optical single-shot readout of a superconducting qubit (2023). ArXiv:2310.16817 [quant-ph].

[33] Zhang, M., Wang, C., Cheng, R., Shams-Ansari, A. & Lončar, M. Monolithic ultra-high-Q lithium niobate microring resonator. *Optica* **4**, 1536–1537 (2017). Publisher: Optica Publishing Group.

[34] Shams-Ansari, A. *et al.* Reduced material loss in thin-film lithium niobate waveguides. *APL Photonics* **7**, 081301 (2022).

[35] Luke, K. *et al.* Wafer-scale low-loss lithium niobate photonic integrated circuits. *Optics Express* **28**, 24452–24458 (2020). Publisher: Optica Publishing Group.

[36] Soltani, M. *et al.* Efficient quantum microwave-to-optical conversion using electro-optic nanophotonic coupled resonators. *Physical Review A* **96**, 043808 (2017). Publisher: American Physical Society.

[37] Zhang, M. *et al.* Electronically programmable photonic molecule. *Nature Photonics* **13**, 36–40 (2019). Number: 1 Publisher: Nature Publishing Group.

[38] Krantz, P. *et al.* A quantum engineer's guide to superconducting qubits. *Applied Physics Reviews* **6**, 021318 (2019).

[39] Holzgrafe, J. C. *Cavity electro-optics in thin-film lithium niobate*. Ph.D. thesis, Harvard University Graduate School of Arts and Sciences (2022).

[40] Puma, E. A. *Towards Scalable Electro-Optic Systems in Thin Film Lithium Niobate Integrated Photonics*. Ph.D. thesis, Harvard University Graduate School of Arts and Sciences (2022).

[41] Duan, L.-M., Lukin, M. D., Cirac, J. I. & Zoller, P. Long-distance

quantum communication with atomic ensembles and linear optics. *Nature* **414**, 413–418 (2001). Number: 6862 Publisher: Nature Publishing Group.

[42] Dauler, E. A. *et al.* Review of superconducting nanowire single-photon detector system design options and demonstrated performance. *Optical Engineering* **53**, 081907 (2014). Publisher: SPIE.

[43] Riedinger, R. *et al.* Remote quantum entanglement between two micromechanical oscillators. *Nature* **556**, 473–477 (2018). Number: 7702 Publisher: Nature Publishing Group.

[44] Jerger, M. *et al.* Frequency division multiplexing readout and simultaneous manipulation of an array of flux qubits. *Applied Physics Letters* **101**, 042604 (2012).

[45] Zeng, B. *et al.* Cryogenic packaging of nanophotonic devices with a low coupling loss < 1 dB (2023).

[46] Zhu, D. *et al.* Integrated photonics on thin-film lithium niobate. *Advances in Optics and Photonics* **13**, 242–352 (2021). Publisher: Optica Publishing Group.

[47] Rosenberg, D. *et al.* 3D integrated superconducting qubits. *npj Quantum Information* **3**, 1–5 (2017). Number: 1 Publisher: Nature Publishing Group.

[48] Lago-Rivera, D., Grandi, S., Rakonjac, J. V., Seri, A. & de Riedmatten, H. Telecom-heralded entanglement between multimode solid-state quantum memories. *Nature* **594**, 37–40 (2021). Number: 7861 Publisher: Nature Publishing Group.

[49] Bhaskar, M. K. *et al.* Experimental demonstration of memory-enhanced quantum communication. *Nature* **580**, 60–64 (2020). Number: 7801 Publisher: Nature Publishing Group.

[50] Fu, W. *et al.* Cavity electro-optic circuit for microwave-to-optical conversion in the quantum ground state. *Physical Review A* **103**, 053504 (2021). Publisher: American Physical Society.

V. METHODS

A. Fabrication

Devices are fabricated on 600-nm x-cut thin-film lithium niobate (TFLN) bonded on 4700 nm of thermally grown oxide on a silicon carrier (NanoLN). The waveguides are defined using negative-tone hydrogen silsesquioxane (HSQ) (FOx-16) by means of electron-beam lithography under 4x-multipass exposure (Elionix F-125). The pattern is then transferred to LN through a physical etching process using Ar^+ ions to form a 325 nm ridge waveguide. We further confirm the thickness of the remaining film by means of an optical profiler (Filmetrics). We used a wet chemical process to clean the resist and redeposited material after the physical etching. The chip is then cladded with 1.4 μm of inductively-coupled plasma enhanced chemical vapor deposition (IC-PECVD) SiO_2. Windows are etched into the cladding oxide and waveguide slab before 40nm of niobium is sputtered onto the chip. The microwave layer is then defined with positive tone propyleneglycol monomethyl etheracetate photoresist (SPR 700-1.0) by means of optical lithography (Heidelberg 150) and transferred to the niobium film using a C_3F_8 physical etch. The etch depth is targeted to be 100nm to ensure that the microwave resonator is fully defined.

B. Microwave Loss Calibration

We extract the microwave losses at the transducer using low-power bidirectional transduction measurements, given that

$$\eta_{MW \rightarrow opt.} = \eta_{opt \rightarrow MW} \qquad (1)$$

$$\eta_{MW \rightarrow opt,meas} = \frac{\omega_o}{\omega_m} \eta_{m,in} \eta_{opt.,out} \eta_{transducer} P_{m,in} \qquad (2)$$

and

$$\eta_{opt. \rightarrow MW,meas} = \frac{\omega_m}{\omega_o} \eta_{opt.,in} \eta_{m,out} \eta_{transducer} P_{opt,in} \qquad (3)$$

where $\eta_{opt,in(out)}$ describe the input (output) optical link gain and $\eta_{m,in(out)}$ describes the input (output) microwave link gain. Optical losses are measured at room temperature

with a powermeter (Thorlabs PM100D) calibrated against an integrating sphere (Thorlabs S140C). It is assumed that optical losses in our measurement network remained nominally constant throughout the experiment.

We extract the microwave losses between the transducer and qubit by comparing the theoretical and measured Rabi frequencies to estimate on chip power at the qubits compared to on chip power at the transducer extracted from bidirectional transduction measurements given that, in the dispersive coupling regime,

$$\Omega_R \approx 2 \frac{g_{q-ro}}{\Delta_{ro}} \frac{P_{avg}}{\hbar \omega_{dr}} \qquad (4)$$

where g_{q-ro} is the qubit-readout resonator coupling strength, Δ_{ro} is the detuning between the qubit and readout resonator, $P_{avg} \approx \frac{1}{.94} f_r t_p$ is the average power arriving at the qubit for peak power P_{pk} at repetition rate f_r and pulse width t_p, and ω_{dr} is the frequency of the qubit drive. For off-resonant drive, like the chevron measurement in Fig. 4d, we expect to measure a rolloff in Rabi frequency

$$\Omega_R' = \sqrt{\Omega_R^2 + \delta^2} \qquad (5)$$

where δ is the detuning between the qubit frequency and driving tone.

C. Transducer Measurement

For independent transducer measurements, a Santec TSL-550 CL band laser operated around 1530 nm is sent to a single-sideband electro-optic modulator. For optical-to-microwave conversion experiments, the modulator is weakly driven by a vector network analyzer (VNA) at the transducer microwave resonator frequency to generate an optical sideband. For microwave-optical conversion experiments, the VNA output is switched to the dilution refrigerator input and used to apply a weak microwave idler to the transducer. The optical pump(s) can be switched to an acousto-optic modulator (AOM) and electro-optic modulator (EOM) for phase locking the optical pump laser to the optical resonator using the Pound-Drever-Hall technique. A DC bias is applied to the transducer bias capacitor by applying a DC voltage to a cryogenic bias-tee (QMC-CRYOTEE-0.218SMA) using a

Keithly 2400 power supply.

D. Qubit Control

Qubit control was implemented using the Xilinx ZCU111+ Radio Frequency System on Chip (RFSoC) with control built using the open-source Quantum Instrument Control Kit (QICK). Qubits could be characterized independently from the transducer by sending in control pulses on a directional coupler after the transducer chip to give a baseline for qubit measurements using 50 ns pulses with 100 μs repetition rate averaged over 1000 experimental shots. This allowed us to establish a baseline for qubit lifetimes (T_1), coherence times (T_2^*), and RF readout fidelities.

E. Optically-Driven Qubit Measurements

In transducer-driven power-Rabi measurements, output power was swept from -108.33 to -107.36 dBm for 100 ns pulse width measurements and converted to voltage units assuming a 50 Ω load. Here, measurements were averaged over 1000 experimental shots.

For transducer driven time-Rabi measurements, output power was held fixed at -115.8 ± 0.4 dBm. Power was regularly checked on a VNA between each frequency flux bias in order to verify that the transducer bias had not drifted. Here, measurements were averaged over 5000 experimental shots.

VI. EXTENDED DATA
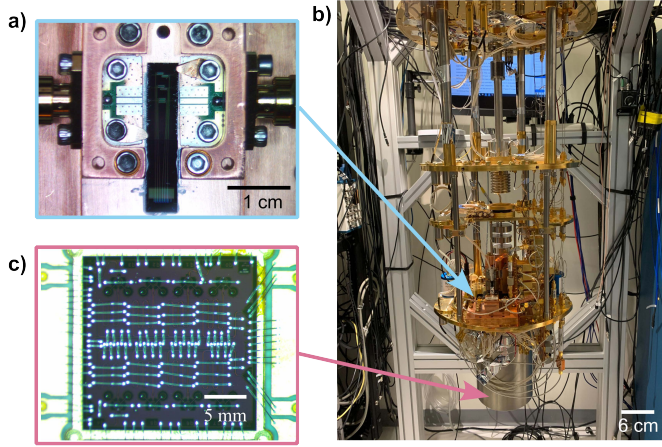

Fig. 6. (a) Our transducer chip is enclosed in copper packaging and wirebonded to a 50 Ω transmission line (Lotus Communication Systems) used to send and receive signals from the transducer using microwave coaxial cables. (b) We optically couple into our device using a fiber grating coupler array mounted to a three-axis attocube positioner. Generated microwave signals are transmitted to the qubit chip (c) which is wirebonded to an electronic carrier and suspended in three layers of magnetic shielding below the mixing chamber plate.
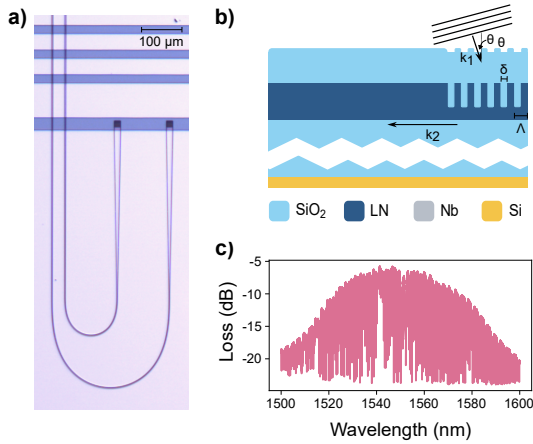

Fig. 8. We simulate the microwave-optical single photon coupling rate, g_0, for (a) fully cladded and (b) plateau etch electrode geometries. (c) We see a 1.4x improvement in single photon coupling rate when comparing the plateau etch to a fully cladded device.

Fig. 7. (a) Optical micrograph of grating couplers etched in TFLN cladded with SiO_2. A Nb alignment grating is created around the couplers in order to help with coupling inside of the dilution refrigerator. (b) Cross section of grating couplers for transducer material stack. Light is coupled into the waveguide according to the phase matching condition $k_2 = k_1 sin\theta + \frac{2\pi n_{eff}}{\Lambda}$ where $k = 2\pi/\lambda$ is the wave-vector in the material propagating at angle θ and gratings are described by pitch Λ and separation δ. (c) Loss per grating measured through our device.

Fig. 9. Schematic for CEO-MOQT and SC qubit measurements. (a) Simplified schematic for microwave→optical conversion and (b) optical→microwave conversion. Here, solid lines correspond to electrical cabling and dotted lines correspond to optical fiber. (c) detailed schematic for the whole measurement system. Transducer components are highlighted in gold. Qubit components are highlighted in pink.

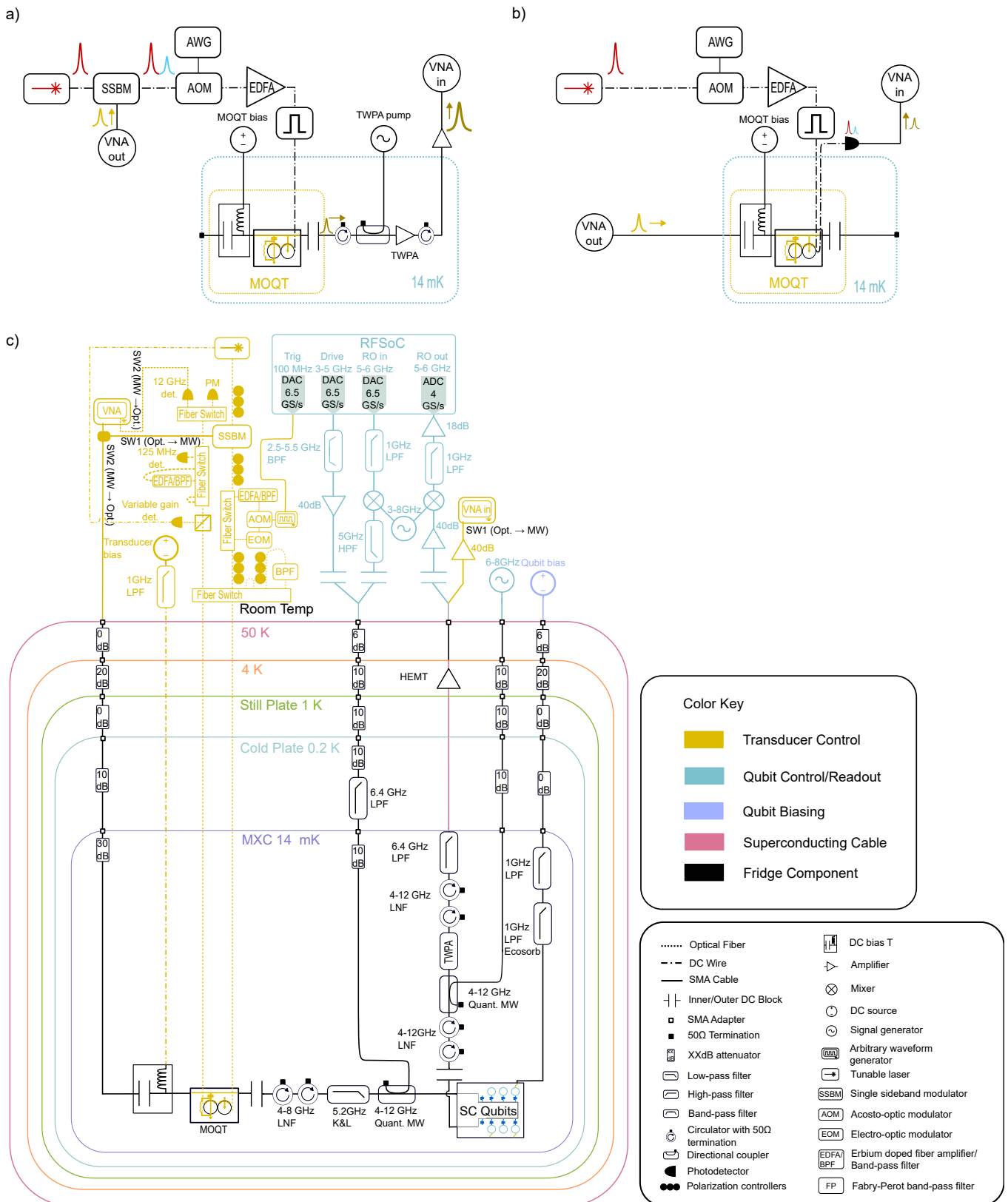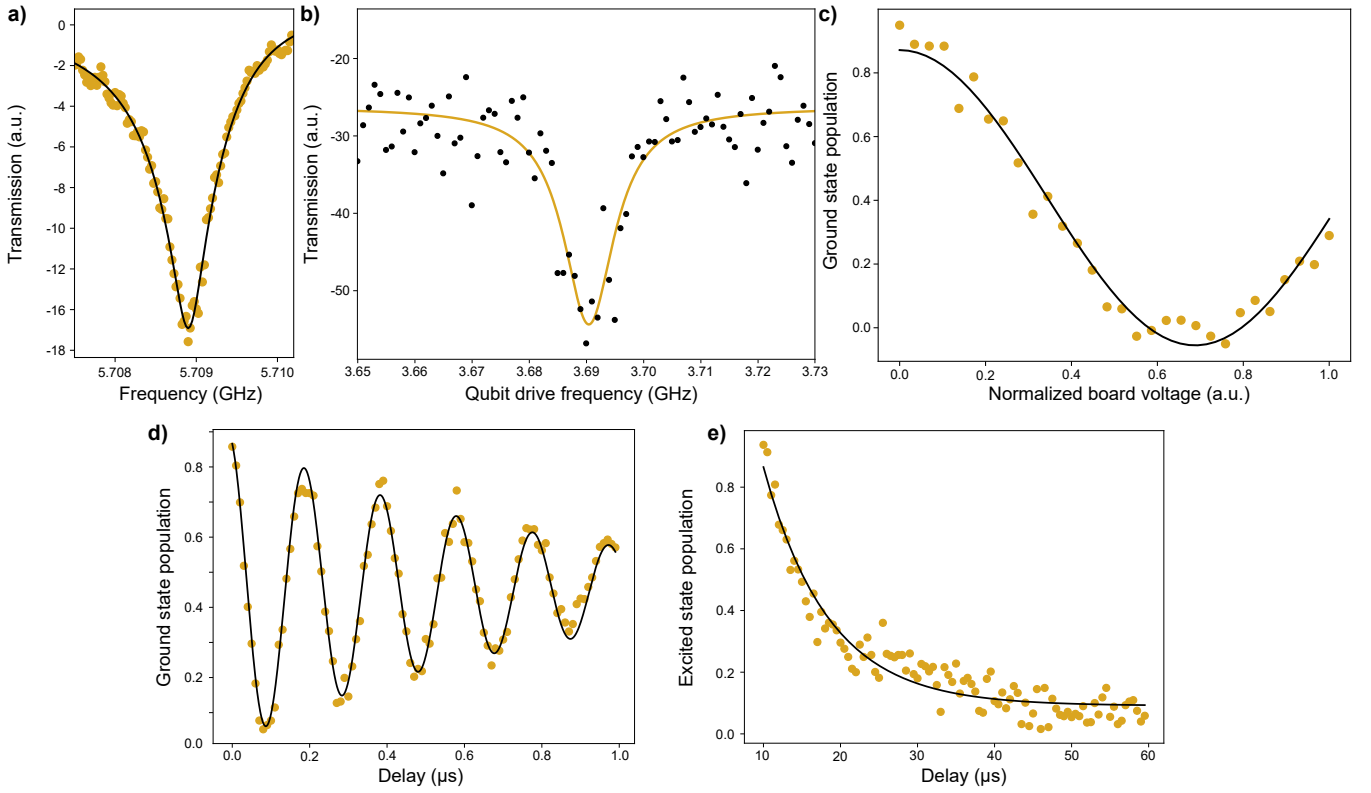Fig. 10. Summary of all-RF qubit bring-up using power domain π-pulses, including (a) readout resonator transmission at 5.709 GHz, (b) qubit spectroscopy when the qubit is flux-biased to 3.690 GHz, (c) power Rabi oscillations reported in arbitrary voltage units, (d) Ramsey measurements, from which we extract a coherence time $T_2^* = 800$ ns, and a lifetime measurement, from which we extract a lifetime of $T_1 = 8$ μs.
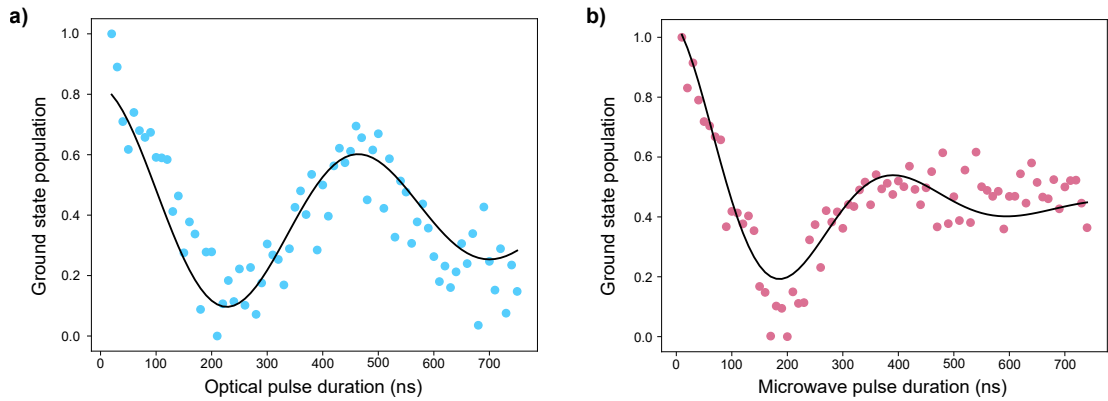
Fig. 11. Comparison of time-Rabi data for (a) transducer-driven qubit measurements ($\tau \approx 800$ ns$\approx T_{2\,RF}^*$) and (b) all-microwave qubit measurements ($\tau \approx 300$ ns$< T_{2\,R}^* F$) for similar microwave power at the qubits ($\Omega_R \approx 2.2$ MHz).
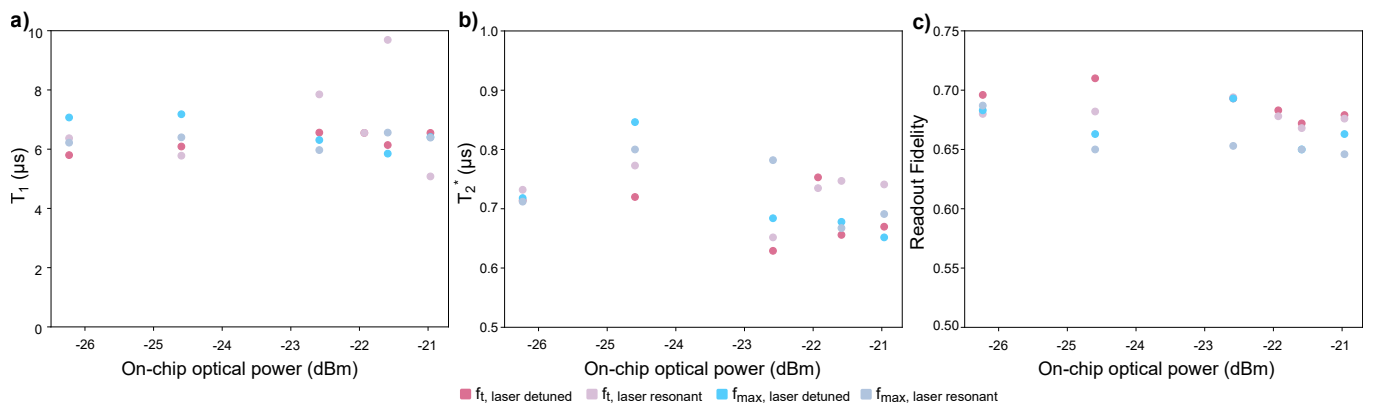
Fig. 12. (a) Qubit lifetime (T_1) and (b) coherence time (T_2^*) as a function of on-chip optical power with a single strong pump field (no optical idler). We see that the qubit lifetimes do not experience significant degradation with increased optical power at the transducer flux bias ($f_{CEO-MOQT}$ = 3.71 GHz) or the qubit maximum frequency (f_{max}=4.571 GHz). (c) Qubit readout fidelity as a function of on-chip optical power in the pump field (no optical idler).

SUPPLEMENTARY INFORMATION

A. System Dynamics

In this article, we describe an electro-optic transducer used to drive a superconducting qubit. In the transducer, the microwave and optical domains are coupled by the Pockel's electro-optic effect to mediate a three-wave mixing interaction

$$\frac{H_0}{\hbar} = \omega_{a_1}\hat{a}_1^\dagger\hat{a}_1 + \omega_{a_2}\hat{a}_2^\dagger\hat{a}_2 + \omega_b\hat{b}^\dagger\hat{b} \tag{6}$$

$$\frac{H_I}{\hbar} = g_{eo}(\hat{a}_1\hat{a}_2^\dagger\hat{b} + \hat{a}_1^\dagger\hat{a}_2\hat{b}^\dagger) \tag{7}$$

Where g_{eo} describes the single-photon coupling rate between the microwave ($\hat{b}$) and optical modes, $\hat{a}_{\{1,2\}}$.

In our device, two hybridized optical resonators are capacitively coupled to a microwave LC resonator. The resulting eigenmodes $a_\pm$ are delocalized from the waveguide modes. An optical pump field on the red optical mode mediates the conversion between the blue optical mode and microwave mode according to the reduced Hamiltonian

$$\frac{H_{red}}{\hbar} = -\Delta_+\hat{a}_+^\dagger\hat{a}_+ + \omega_m\hat{b}^\dagger\hat{b} + g(\hat{b}^\dagger\hat{a}_+ + \hat{b}\hat{a}_+^\dagger) \tag{8}$$

in a frame rotating at laser frequency $\omega_L \approx \omega_-$, where $\hat{a}_\pm$ are the eigenmodes of the hybridized optical resonator at frequencies $\omega_\pm$, $\Delta_+ = \omega_L - \omega_+$ is the detuning between the laser field ω_L and the blue optical mode ω_+, $\hat{b}$ is the microwave mode at frequency ω_m, and g is the pump enhanced coupling term

$$g = \sqrt{\bar{n}_-}g_{eo} \tag{9}$$

Where $\bar{n}_-$ describes the number of red pump photons defined by

$$\bar{n}_- = \frac{\kappa_{e,-}}{\Delta_-^2 + (\kappa_-/2)^2}\frac{P_{pump}}{\hbar\omega_L} \tag{10}$$

For total (extrinsic, intrinsic) loss rate $\kappa_{-(e,i)}$, detuning $\Delta_- = \omega_L - \omega_-$, and pump power P_{pump}. The microwave signal generated by our transducer at ω_m is sent to a superconducting qubit ($\hat{q}$) via coaxial cable to allow for modular integration between the two sub-systems. We use a flux-tunable split-transmon qubit dispersively coupled to a readout resonator (ω_{ro}). For a qubit-cavity coupling rate g_{q-ro} and qubit (cavity) loss rates $\kappa_{q(ro)}$, the system can be described by

$$\frac{H_{q-ro}}{\hbar} = \left(\omega_r + \frac{g^2}{\Delta}\hat{\sigma}_z\right)\left(a^\dagger a + \frac{1}{2}\right) + \frac{\omega_a}{2}\hat{\sigma}_z \tag{11}$$

in the dispersive coupling regime where $g_{q-ro} >> \kappa_q, \kappa_{ro}$. Here, $\Delta_q = \omega_{ro} - \omega_q$ is the detuning of the readout resonator from the qubit frequency and σ_z is the Pauli z operator describing population exchange between the qubit ground and excited states. This allows us to measure the excitation generated by the resonant transducer signal by measuring the transmission of a readout pulse which we generate at room temperature.

B. Electro-optic coupling rate

We can derive the single photon coupling rate in the transducer from our three-wave mixing interaction given

$$H_I = g_{eo}(\hat{a}_1 \hat{a}_2^\dagger \hat{b} + \hat{a}_1^\dagger \hat{a}_2 \hat{b}^\dagger) \tag{12}$$

so the interaction of an optical photon $\hat{a}_1$ with microwave photon $\hat{b}$ produces optical photon $\hat{a}_2$ such that $\omega_{a_2} = \omega_{a_1} + \omega_b$ and the decay of photon $\hat{a}_2$ to $\hat{a}_1$ and $\hat{b}$ with the same energy conservation requirement.

Here, g_{eo} is derived from the interaction energy due to microwave field modulating the index of refraction of the optical resonator due to electro-optic effect, which changes $\sim 1/\epsilon$ for the applied microwave field. Thus, we describe the interaction in terms of the inverse permittivity matrix η and optical displacement field D_0. For our system, this is defined by the crystal axis of the LN waveguide and resulting electric permittivity and the electric field strength in the waveguide described by

$$H_I = \frac{1}{2\epsilon_0} \int_{LN} dV \sum_{ij} \Delta\eta_{ij} D_{oi} D_{oj} \tag{13}$$

$$= \frac{\epsilon_0}{2} \int_{LN} dV \sum_{ij} \Delta\eta_{ij} \epsilon_{ii} \epsilon jj E_{oi} E_{oj} \tag{14}$$

(which follows from $D = \epsilon E + P$)

Assuming fields are aligned along the crystal coordinates and substituting the electro-optic coefficient tensor r for $\Delta\eta_{ij} = \sum_{ijk} r_{ijk} E_{\mu k}$, and defining the microwave and optical fields as $E_\mu = (e_b b + h.c)$, $E_0 = (\hat{e}_{\hat{a}_1}\hat{a}_1 + e_{\hat{a}_2}\hat{a}_2 + h.c)$ it follows that

$$H_I = \epsilon_0 \int_{LN} dV \sum_{ij} \epsilon_{ii} \epsilon_{jj} r_{ijk} (\hat{e}_{a_1 i} + \hat{e}_{\hat{a}_2 j}^* \hat{e}_{bk} \hat{a}_1 \hat{a}_2^\dagger b + h.c) N_{\hat{a}_1} N_{\hat{a}_2} N_{\hat{b}} \tag{15}$$

As derived in[9]. Here, only energy conserving terms are maintained. Each electric field is normalized to zero point energies such that

$$N_m = \sqrt{\frac{\hbar\omega_m}{2\epsilon_0 \int dV \sum_{ij} \hat{e}_{ij} \hat{e}_{mi} \hat{e}_{ij}}} \tag{16}$$

In our device, the primary field contribution is along the r_{33} TFLN crystal axis, so we can simplify the electro-optic tensor such that

$$g_{eo} = \epsilon_0 n_e^4 r_{33} \int_{LN} dV \hat{e}_{\hat{a}_1} \hat{e}_{\hat{a}_2}^* \hat{e}_{\hat{b}} N_a N_b N_c \tag{17}$$

We can thus use this to simulate the expected microwave-optical coupling rate g_{eo} by examining the microwave field in the waveguide in a COMSOL multiphysics simulation. This can be simplified by considering the electro-optic response in the device.

In this work, we describe a ring resonator with circumference l (resonant condition $l = \frac{k\lambda_0}{n}$, where k is the mode index, λ_0 is the free space wavelength, and n is the (effective) refractive index).

resulting in optical modes with frequencies $f_{0,k} = \frac{kc}{ln}$. Changes to index of refraction $n \to n + \Delta n$ results in

$$f'_{0,k} = \frac{kc}{l(n - \Delta n)} \approx f_{(0,k)} \left(1 - \frac{\Delta n}{n}\right) \tag{18}$$

An electric field E inside the optical waveguide linearly shifts the refractive index due to the Pockel's electro-optic effect, so for

electric field applied along one direction

$$n_{LN}(E) \equiv n_{LN} - \frac{1}{2} r n_{LN}^3 E \tag{19}$$

where $r = -\frac{2}{n^3} \frac{dn}{dE}|_{E=0}$ is the electro-optic coefficient. Along the z-axis of LN, $r = r_{33} \approx 30 pm/V$, $n_{LN} = n_e = 2.14$, and the electric field is highly uniform within the waveguide so we neglect the cross sectional variation of E yielding the electro-optic susceptibility

$$\frac{G_i}{2\pi} = \frac{n_e^2 r_{33} f_0 \alpha \Gamma}{2|V/E|} \tag{20}$$

where α is the fraction of the ring covered by electrodes, $\Gamma = \frac{\delta n}{\delta n_{LN}} \frac{n_L N}{n}$ is susceptibility of effective mode index in waveguide to changes in refractive index (this is essentially a confinement factor, with $\Gamma \approx 1$)

This results in a vacuum coupling strength

$$\frac{g_i}{2\pi} = G_i V_{ZPF} \tag{21}$$

From here, we can define the zero-point fluctuations $V_{ZPF} = \langle 0|V^2|0\rangle$ of the LC resonator by finding the RMS voltage in an LC resonator with capacitance C and energy equal to vacuum energy of the resonator,

$$CV_{ZPF}^2 - \frac{1}{2}\hbar\omega_m \tag{22}$$

yielding

$$g_i = \frac{n_e^2 r_{33} w_0 \alpha \Gamma}{2|V/E|} \sqrt{\frac{\hbar\omega_m}{2C}} \tag{23}$$

We compare a fully cladded device (Fig. 8a) to a device where we etch down the cladding and slab to create a "plateau" around the waveguide and gate the electrodes directly with the z axis of the LiNbO$_3$ crystal (Fig. 8b). We simulate the electric field response in COMSOL multiphysics and infer device parameters to predict a 40% improvement in g_{eo} for a "plateau etch" geometry when compared to a fully cladded device. This is due to the stronger electro-optic field overlap in the waveguide and avoiding dielectric losses in the SiO$_2$ cladding (Fig 8c).

C. Measurement Setup

The measurement setup is depicted in Fig 9, with simplified schematics for Opt.→MW transduction depicted in Fig. 9a and MW→Opt. transduction depicted in Fig. 9b. For MW→Opt. transduction (Fig 9a), a strong pump laser (red) at ω_- is modulated by a vector network analyzer (VNA) at a single sideband modulator (SSBM) near the microwave resonator frequency (yellow) to generate a weak optical sideband at ω_+ (blue). The field field can then be modulated by an acousto-optic modulator (AOM) driven by an arbitrary waveform generator (AWG) to pulse the input optical fields. These are then amplified by an erbium doped fiber amplifier (EDFA) and filtered by a band-pass filter (BPF) to compensate for losses in the bulk modulators. The optical fields are then coupled into the devices with a fiber grating array and interact at the transducer to generate a microwave tone that can be measured on the VNA after amplification at 15 mK by a Josephson traveling wave parametric amplifier (TWPA), 4K by a high electron mobility transistor (HEMT), and room temperature by low noise amplifiers. In (b), a strong pump (red, ω_-) is sent to the AOM in order to pulse, amplify, and filter the field before interacting with a microwave tone (yellow) generated by the VNA at the transducer. The beatnote between up-converted optical field (blue) and pump are measured at a calibrated

detector to measure the converted optical power.

The full experiment setup is depicted in Fig. 9c. For independent transducer measurements, qubit components are treated as loss. A directional coupler before the qubits allows us to characterize the qubits independent of the transducer.

For independent qubit measurements, a qubit driving pulse at the qubit frequency is generated by the RFSoC and transmitted to the qubit via a directional coupler (QMC-CRYOCOUPLER-20) after filtering and amplification. The qubit can be DC flux biased between 3.25 and 4.5 GHz using a Keithly 2400 power supply. A readout pulse can then be generated at the qubit readout resonator frequency to readout out the qubit state after amplification. We amplify first at base temperature using a TWPA, then at 4K using a HEMT, before finally amplifying at room temperature in two steps using low noise amplifiers before (ZX60-83LN-S+) and after (RF Bay LNA-2500) mixing our signal down to our board frequency using a double balanced mixer (ZX05-63LH-S+).

For transducer-driven qubit measurements, the readout pulse is generated at the RFSoC and directed to the readout resonator on a separate transmission line and collected at the RFSoC after amplification and analog processing. The transduced tone and the readout pulse are separated at the output of the dilution refrigerator to measure optical-microwave transduction, using a vector network analyzer (VNA), and qubit excitation, using the RFSoC, simultaneously. Each measurement is averaged over many (1000-10,000) experiment shots. The outputs are split on a 3dB coupler (QMC-CRYOCOUPLER-20) to allow for simultaneous monitoring of the transducer and qubit outputs.

We use 40 dB of isolation (QMC-CIRC-4-12) between our system components (transducer, qubits, TWPA). An inner/outer DC block (Narda-Miteq 4563) prevents DC flux leakage from the transducer and qubit bias.

We perform qubit power-Rabi measurements by keeping a fixed optical pulse width and pump power (ω_-) while linearly increasing the optical power in the blue sideband (ω_+) arriving at the transducer. A long relax-delay compared to the optical pulse width allowed us to maintain a low bath temperature (T≈14 mK). We report measurements for a 100 ns optical pulse, which we expect to result in a corresponding microwave pulse width.

For transducer-driven time-Rabi measurements we keep fixed power in the optical pump and idler and sweep the optical pulse width in order to change the width of the microwave pulse arriving to the qubits. The transducer output power is fixed to -115.8 ± 0.4 dBm. The flux bias is swept to bias the qubit to different frequencies in order to measure the qubit excitation relative to the transducer frequency in a chevron-type measurement. This allows us to ensure that the qubit is biased at the transducer frequency.

D. Transducer packaging

The transducer is enclosed in a copper box and wirebonded to a 50 Ω waveguide (Fig. 6a). We couple into the device with an optical grating coupler array (Fig. 6b) using three axis attocube controllers on the mixing chamber plate of our dilution refrigerator.

Optical grating couplers (Fig. 7a) are created on chip by etching a 15×15 μm pad with teeth with period Λ = 750 nm with separation of δ = 562 nm. This results in a phase matching condition of $k_2 = k_1 \sin\theta + \frac{2\pi n_{eff}}{\Lambda}$ where $k = 2\pi/\lambda$ is the wavevector in the material propagating at angle $\theta = 8°$. A cross section of the grating couplers is drawn in Fig. 7b. In our system, transmission is optimized for operation at 1560 nm with a 30 nm 3 dB bandwidth (Fig 7c).

We etch a niobium alignment pattern to facilitate blind coupling in our dilution refrigerator (Fig. 7a). The niobium ground plane is etched away between the grating couplers and device region, leaving ~ 7.5 mm of exposed silicon dioxide between the optical coupling and transducer regions. We expect this, combined with enclosed packaging and the low kinetic inductance of niobium, can help mitigate optically-induced noise generation in our superconductor. Optical insertion loss measured at peak grating coupler transmission was ~ 4.5 dB/facet; however, the mode pair described here was slightly outside of the grating coupler bandwidth, resulting in an insertion loss of ~ 10 dB/facet.

The qubit devices are wirebonded to a PCB and packaged in a puck that sits inside of three levels of magnetic shielding thermalized to the mixing chamber plate (Fig. 6c).

It is expected that the dominant source of noise in our system is due to optically-induced quasi-particle generation in our superconducting microwave resonator resulting in the breaking of superconducting Cooper pairs. To mitigate these effects, we use a low-kinetic inductance superconducting material (niobium) with kinetic inductance ($L_k \approx 0.5$ pH/sq) and enclose our device in a copper box to reduce scattered light arriving at our transducer. We also use pulsed optical excitation to mitigate "fast" noise dynamics in the system due to bath heating effects[50]. This allows us to mitigate red-shifting and broadening in our output microwave signal imposed by changes in our resonator inductance.

E. RF Qubit Characterization

The qubit is initially characterized in the RF domain using the Xilinx ZCU111 RFSoC. Measurement control was written using the Quantum Instrument Control Kit (QICK). With the exception of time-Rabi measurements (where pulse width was swept), we use 50 ns Gaussian pulses with 100 µs repetition rate averaged over 1000 shots. Measurement fidelity was evaluated as F=71.2% using successive single shot π- and 0-pulse measurements.

For readout resonator spectroscopy, we measure the transmission of a readout pulse through the qubit measurement lines to find the resonance frequency (Fig. 10a). We measure at swept output readout pulse powers to ensure that we are operating in the dispersive coupling regime. Similarly, we perform qubit spectroscopy by transmitting successive driving pulses at the qubit frequency and readout resonator frequency to readout the qubit state (Fig. 10b). We then complete qubit power Rabi measurements to find the qubit π-pulse voltage, and then perform lifetime (T_1) and coherence time (T_2^*) measurements by sending π-pulses and successive $\frac{\pi}{2}$-pulses at the qubit frequency. We extract a $T_1 \approx 8$ µs and $T_2^* \approx 800$ ns.

Finally, we can measure qubit RF-driven time-Rabi oscillations and compare them to the case of optically-driven time-Rabi oscillations. Here, for similar on chip microwave powers, we see a larger characteristic time constant decay $\tau_{Rabi} \approx 220$ ns in RF-driven time-Rabi oscillaiton measurements, compared to a characterstic decay of $\tau_{Rabi} \approx 800$ ns for the optically-driven time-Rabi oscillations. This suggests in the optically-driven time-Rabi case, our decay time is limited by our qubit $T_2^* = 800$ ns, whereas for the RF-driven case there is added noise in our room temperature measurement chain that could be reducing the coherence time of our qubits for long RF pulses.

F. Optically-induced decoherence

We characterize the qubit performance while optically pumping the transducer with a single strong pump field (not generating coherent microwave signals). This allows us to characterize qubit performance (T_1, T_2^*, RO fidelity) under the effect of thermal bath heating or microwave noise generation due to our optical pump.

We characterized the qubits while flux biased to the transducer frequency (f_{ceo} =3.71 GHz) and at the maximum frequency (f_{max} =4.57 GHz) while the laser was parked on resonance with the red mode of the transducer and while detuned from resonance. We observed little effect of the transducer pump on the qubit lifetimes under optical pumping, and qubit lifetimes (Fig. 12a) and coherence time (Fig. 12b) remained fairly consistent with the qubit performance independent of the transducer. Our measurements therefore indicate that the optical powers required to drive the transducer do not limit the T_1 of our qubits (at least to ~9µs). It is noted that this baseline characterization occurred at 0V flux bias, which corresponds to a qubit frequency of 4.2 GHz.

Baseline qubit readout fidelities before connecting the transducer and qubit with coaxial cables were measured as $F \approx 72\%$ with successive single shot measurements. The transducer and qubits were then connected in a later cooldown, where we characterized qubit performance while optically pumping the transducer. We measured a similar base readout fidelity ($F \approx$

70%) when the two systems are combined. We see a decay of the RO fidelity above -25dBm on chip optical pumping power (Fig. 12c). As a result, we targeted average optical powers $P_{avg} \approx -30$dBm for our combined experiment in order to keep readout fidelity as high as possible.

It is noted that readout fidelity in this system was highly dependent on the TWPA pump frequency, mixer image frequency, and amplifier bias, indicating system degradation due to room temperature qubit and TWPA control electronics. Further improvements to the system are needed to verify whether the transducer could impose further challenges to qubit readout.

G.   Optically generated entanglement in SC processor nodes

In the DLCZ remote entanglement scheme drawn in Fig. 5a, two transducers in two separate nodes are pumped to generate correlated microwave-optical photon pairs. In this case, the transducer is pumped on the blue optical mode (ω_-) to generate photon pairs via spontaneous parametric down conversion (SPDC) according to

$$H/\hbar = -\Delta_- \hat{a}_-^\dagger \hat{a}_- + \omega_m \hat{b}^\dagger \hat{b} + g(\hat{b}^\dagger \hat{a}_-^\dagger + \hat{b}\hat{a}_- \tag{24}$$

for detuning $\Delta = \omega_+ - \omega_-$ and g is the pump-enhanced electro-optic interaction term.

The two paths are entangled by a beamsplitter before the devices. In a weak pumping regime ($C << 1$ and multi-photon events $p_{multi} << 1$), we can approximate the state in each node (A,B) as

$$|\psi\rangle_{A,B} \sim |0_m 0_o\rangle_{A,B} + \sqrt{p}|1_m 1_o\rangle_{A,B} \tag{25}$$

where p is the pair generation probability and $\{m, o\}$ denotes the microwave and optical resonators, respectively. For a low microwave loss rate compared to the optical loss rate ($\kappa_m << \kappa_o$), the internal pair generation probability is given by $p = \frac{4g_{eo}^2}{\kappa_o}N$, where g_{eo} is the single photon electro-optic interaction rate and N is the number of photons in the pump pulse. The optical outputs of the two nodes can be interfered on a beamsplitter to erase the which-path information. The detection of a single optical photon at the detectors will herald the creation of the entangled bell state

$$|\Psi^\pm\rangle = \frac{1}{2}\left(|0_m\rangle_A|1_m\rangle_B \pm e^{i\Delta\phi}|1_m\rangle_A|0_m\rangle_B\right) \tag{26}$$

The bell state can be transferred to a SC qubit network through a transmission line for further processing.

We can characterize the practicality of this method by examining metrics of entanglement generation rate R_{ent} and link fidelity F. Our entanglement generation is described by $R_{ent} = \eta_{opt}pR$ for total detection efficiency η_{opt} (including coupling, propagation, and pump filter losses), pair generation probability p, and attempt repetition rate R. In general, the repetition rate is limited by the time required to reset the microwave resonator between entanglement attempts; we estimate $R < \frac{\kappa_m}{10} \approx 1$ MHz. The link fidelity between the microwave and optical nodes is described by

$$F = |\Psi_{ideal}^\pm|\Psi_{real}^\pm|^2 = 1 - p_{multi} - 2P_m - \frac{3}{2}P_{loss} - P_{false} - P_{phase} \tag{27}$$

for a given probability of multi-photon events (p_{multi}), microwave noise photons (P_m), transmission loss (P_{loss}), false detection events (P_{false})), and phases errors (P_{phase})).